



# Identification of the heat source and thermal material model parameters for the laser engineered net shaping

Lucyna Hajder<sup>1</sup> , Tao Zhang<sup>2</sup> , Vu Nguyen<sup>3</sup> 

<sup>1</sup> AGH University of Science and Technology, al. Mickiewicza 30, 30-059 Krakow, Poland.

<sup>2</sup> Institute for Frontier Materials, Deakin University, 75 Pigdons Road, Waurin Ponds VIC 3216, Australia.

<sup>3</sup> Commonwealth Scientific and Industrial Research Organisation (CSIRO), Manufacturing, Clayton, VIC 3168, Australia.

## Abstract

The research's primary goal is to identify the heat source and thermal material model parameters for the numerical simulation of the laser engineered net shaping (LENS). Inconel 718 was selected as a case study for the current investigation. The LENS process's numerical model was developed within commercial finite element software and was used as a direct problem model during the parameter identification stage. Experimental data were obtained based on a rectangular-shaped sample with thermocouples located under the based material surface. The recorded thermal profiles were used to establish a goal function for the parameter identification stage. As a result, parameters describing the melt pool geometry during the additive manufacturing, as well as thermal coefficients describing interactions between the sample material and surrounding/base material, were determined.

**Keywords:** additive manufacturing, finite element analysis, heat source model, thermal analysis

## 1. Introduction

One of the most advanced technologies for manufacturing products with complex spatial structures, especially in low-volume production, is an additive manufacturing (AM). Year by year, a significant rise in AM system sales has been presented in numerous market reports (Wohlers et al., 2020).

The first references to additive manufacturing concepts were made in the 1980s and are related to Hideo Kodama (1981). He was one of the first to propose a single-beam laser curing approach. Since then, the list of additive manufacturing technologies dedicated to different materials has grown significantly (Jiménez et al., 2019) and there are now many classes and categories of AM technologies. If the material's physical

state is taken into account, there are solid-, powder- and liquid-based approaches (Petrovic et al., 2011). Commonly used solutions fall into the following categories, e.g., vat photopolymerization, binder jetting, material jetting, material extrusion, powder bed fusion, direct energy deposition, or sheet lamination. For metals, AM processes can be specified in two major groups: powder bed fusion based technologies (PBF) and directed energy deposition (DED) based technologies.

It should also be mentioned that not only is the process itself being developed, but also metallic materials for AM are under investigation to provide and introduce solutions for practical applications (Bajaj et al., 2020). The development of AM technological parameters is not a trivial task as various issues have to be addressed, e.g., porosity, lack of fusion (LOF), microcracks, hot-tears

\* Corresponding author: lhajder@agh.edu.pl

ORCID ID's: 0000-0003-0644-7893 (L. Hajder), 0000-0002-1820-7128 (T. Zhang), 0000-0001-6420-2312 (V. Nguyen)

© 2022 Authors. This is an open access publication, which can be used, distributed and reproduced in any medium according to the Creative Commons CC-BY 4.0 License requiring that the original work has been properly cited.

etc. (Brennan et al., 2020). At the same time, layering and different temperature gradients lead to strong inhomogeneities and anisotropic properties of AM parts (Calandri et al., 2019; Pereira et al., 2021). That is why a series of time-consuming tests are needed to design a robust additive manufacturing process using the selected technology. They are expensive as they have to be carried out in the laboratory and then under semi-industrial conditions. For this reason, computer-aided technology design solutions are used more often since they reduce the time and costs of research; however, they have to be adequately developed to replicate material behaviour under particular AM process conditions, e.g., laser engineered net shaping (LENS), reliably.

LENS is one of the technologies where a laser-based system streams and melts the metallic powder at the substrate/base material layer by layer. In this case, powder particles are provided by the nozzle system and directed towards the base material located at the moving table. The laser remains stationary and melts the powder near the top of the deposited layer while the material is added. LENS fabricated parts can have thin walls and a high depth-to-diameter aspect ratio but are still affected by the common processing parameters (such as laser parameters) and many other factors (such as scan speed and powder feed rate) (Izadi et al., 2020). That is why it is essential to understand and control process parameters during fabrication, and the role of the computer-aided technology design approaches is more frequently used in this investigation (Stender et al., 2018; Ye et al., 2006).

Therefore, identification of the heat source and thermal material model parameters for the reliable LENS simulations is performed within the work based on experimental observations and measurements since this was not addressed in depth in the previously quoted articles.

## 2. Experimental investigation

To provide sufficient data for the LENS numerical model identification stage, a dedicated experimental setup was developed. The proposed sample final shape is shown in Figure 1 and is composed of 32 layers of Inconel 718 that were subsequently deposited in one way. The laser with 275 W power was used to deposit 0.41 mm of the material in a single pass. The moving table traverse speed was set to 6.77 mm/s. Considering the sample length, one layer of the material is deposited during a period of 3.75 s. Additionally, an interval between the deposition of subsequent layers was set to 1.2 s. The material is deposited on a substrate also made of Inconel 718 with a thickness of 7 mm. To measure the temperature profiles during the process, three thermocouples were inserted into the based material and located approx. 1 mm from the top surface. One thermocouple is located near the centre of the specimen, while the other two are on both sides, at a distance of 11 mm. The exact positions of the thermocouples are shown in Figure 1.

The temperature profiles recorded during the AM process are presented in Figure 2.

The TC1, TC2 and TC3 lines in Figure 2 illustrate the temperature evolution in the above-presented measurement points. To some extent, differences in temperature profiles may occur due to the spatial arrangement of thermocouples (e.g. localization under the surface, size of holes etc.). Similar temperature profiles are observed at the points close to the sample edges. As expected, the highest temperatures are recorded in the middle of the sample. Data from Figure 2 were then used as input for the finite element model parameters identification operation.

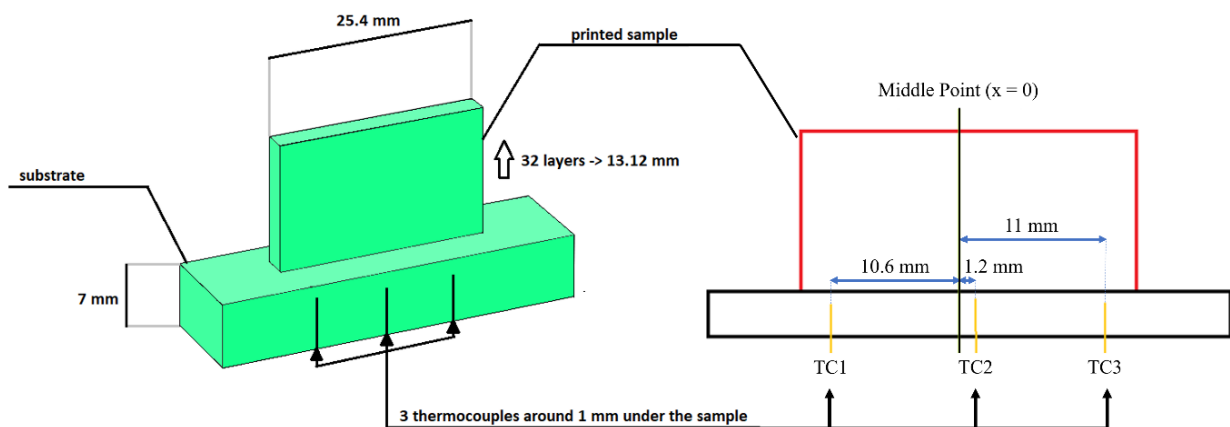


Fig. 1. Dimensions of the AM sample and substrate made from Inconel 718 with exact positions of the thermocouples

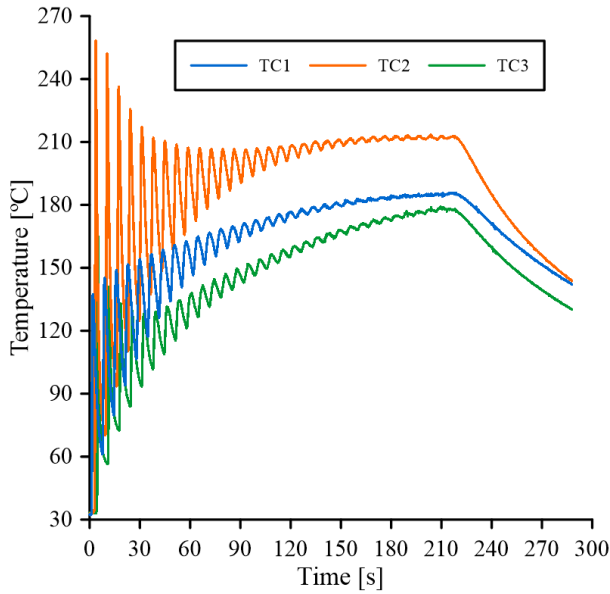


Fig. 2. Temperature profiles recorded during the deposition process

### 3. LENS numerical model

The numerical model requires a specific technique for finite element activation to recreate the nature and conditions occurring in the material during the LENS process. In this case, two approaches are considered in the literature: the passive and inactive methods (Chua et al., 2019). The former assumes that the elements that represent the sample are included in the model at the beginning of the analysis but are passive; therefore, their properties do not affect the rest of the model. The elements remain passive until the laser passes over a specific point. After that, the element is activated, and the thermophysical properties are considered during the subsequent steps of the simulation. This method does not require additional equation renumbering and thus the implementation is straightforward. The former approach classifies elements into active and inactive ones according to the predefined laser path. Therefore, only active elements are assembled as part of the model, while the inactive elements are generated but do not play any role in the simulation until their status is not switched on as presented in Figure 3.

The element progressive activation method is thus used in the current work as described in (Bhandari & Lopez-Anido, 2020). The approach is based on the two major user subroutines. The first is used to activate finite elements, while the second controls the volume fraction increase before its activation. The

approach provides more accurate results than the passive element solution, however, it is more time-consuming (Malmelöv, 2016). The laser movement path, its velocity, heat transfer coefficients, and heat source parameters have to be defined for the current model to provide reliable results. The definition of the latter element, namely the heat source, is particularly important. The most commonly used model to describe the heat source characteristics during the welding operations is the one proposed by Goldak et al. (1984). In this case, the description of the power distribution gives some technical difficulties from the numerical point of view. The finite element mesh is often not fine enough to define a complex welding pool shape. Moreover, the laser energy is used to melt the material of the deposited layer and therefore is transmitted only partially to the base (Chiumenti et al., 2010). With that, it is not a trivial task to obtain an accurate temperature of the deposited material at the welding pool area. The welding pool characteristics depend on four parameters that define a double ellipsoid model, as shown in Figure 4.

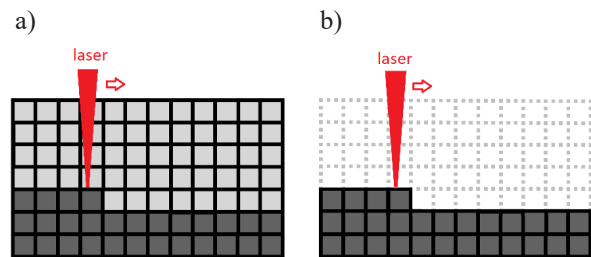


Fig. 3. Techniques for elements activation: a) passive activation; b) inactive activation

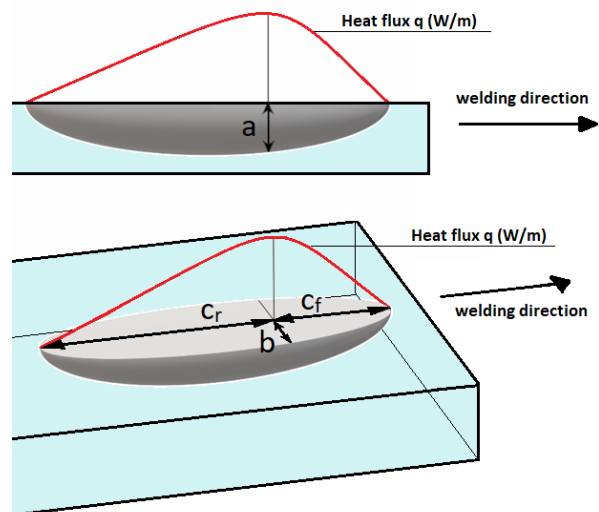


Fig. 4. Parameters of Goldak heat source model incorporated into finite element simulation

Therefore, the heat source model parameters are identified in the current work based on the temperature measurements by the thermocouples (Fig. 1) using the classical analytical approach (Fu et al., 2015).

In Goldak model, the volumetric heat flux density in the front part  $q_f(x', y', z', t)$  and rear part  $q_r(x', y', z', t)$  is described by the two equations:

$$q_f(x', y', z', t) = \frac{6\sqrt{3}f_f Q_w}{abc_f \pi \sqrt{\pi}} \exp\left(-\frac{3x'^2}{a^2}\right) \exp\left(-\frac{3y'^2}{b^2}\right) \exp\left(-\frac{3z'^2}{c_f^2}\right) \quad (1)$$

$$q_r(x', y', z', t) = \frac{6\sqrt{3}f_r Q_w}{abc_r \pi \sqrt{\pi}} \exp\left(-\frac{3x'^2}{a^2}\right) \exp\left(-\frac{3y'^2}{b^2}\right) \exp\left(-\frac{3z'^2}{c_r^2}\right) \quad (2)$$

where:  $Q_w$  – the total power;  $a, b, c_f, c_r, f_f$  and  $f_r$  – welding pool parameters presented in Figure 4.

The constants describing how much of the total heat is transferred to the relevant parts of the pool  $f_f$  and  $f_r$  are usually described by the ratio of 60 : 40 and must satisfy the dependence  $f_f + f_r = 2$  (Denga et al., 2007; Kik, 2020). These values can also be obtained from equations:

$$f_f = \frac{2c_f}{c_r + c_f} \quad (3)$$

$$f_r = \frac{2c_r}{c_f + c_r} \quad (4)$$

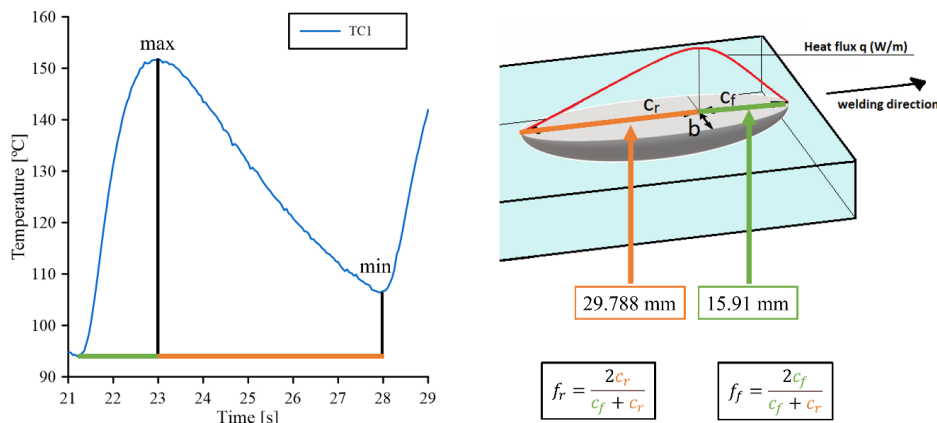


Fig. 5. Illustration of the example for  $f_f$  and  $f_r$  parameters calculation procedure

Table 1. Parameters of the welding pool for Goldak heat source

$a$ [mm]	$b$ [mm]	$c_f$ [mm]	$c_r$ [mm]	$f_f$	$f_r$
0.3	0.25	0.3	0.3	1.3	0.7

By analysing the temperatures and time length (based on the laser velocity) of the front and rear part of the pool at the measured points (as presented in Fig. 5), the above constants were determined as 1.3 and 0.7, respectively.

General values for depth, width, and length of the pool were calculated based on the laser power, volumetric heat flux density, heat transport through the sample (conduction), and material properties based on the non-linear heat transfer equation (Bergman et al., 2011):

$$k \left( \frac{\partial^2 T}{\partial x^2} + \frac{\partial^2 T}{\partial y^2} + \frac{\partial^2 T}{\partial z^2} \right) + Q_{laser} = \rho c_p \frac{\partial T}{\partial t} \quad (5)$$

where:  $Q_{laser}$  – the internal heat source rate;  $k, \rho, c_p$  – the conductivity, density, and specific heat of the plate material, respectively.

The summary of calculated parameters for Goldak model in the investigated LENS process is presented in Table 1.

The 3D models of the deposited sample and the base were created with the finite element method considering coupled thermal and mechanical analysis. The model was discretized with the use of cubic finite elements for the base and the sample material. The influence of the mesh density on the welding pool was examined during three simulations (for fine, medium, and coarse mesh – Table 2) to obtain the optimal size of the elements in the mesh. Element sizes were selected on the basis of a deposition thickness 0.41 mm. If the mesh is too fine, the calculations provide results in a longer time, and the output file takes up more disc space.

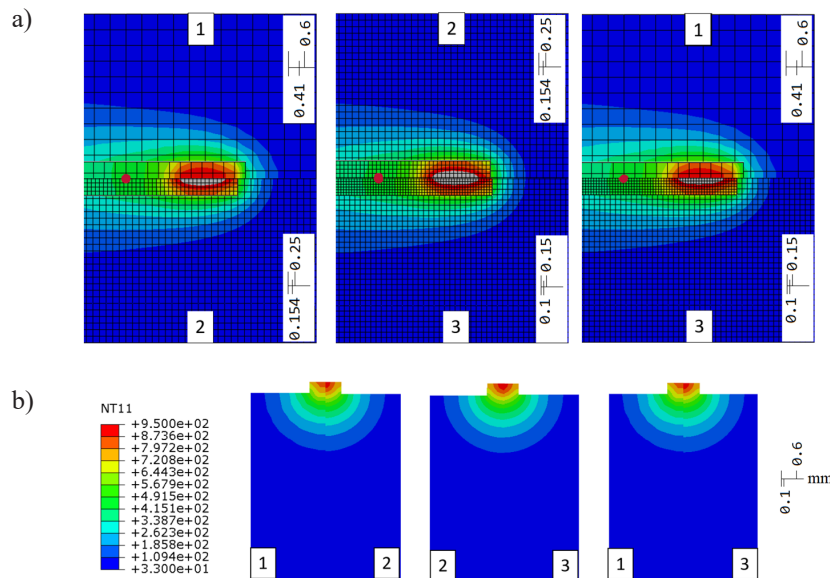
**Table 2.** Element sizes in three simulations showing the influence of mesh density on the welding pool

	Coarse mesh [mm] – 1	Medium mesh [mm] – 2	Fine mesh [mm] – 3
Sample	0.41	0.15375	0.1025
Base	0.6	0.25	0.15

Examples of the results obtained for the three mesh densities of the substrate and sample models are presented in Figure 6. Half of the models with different mesh setups were arranged together for an easier comparison.

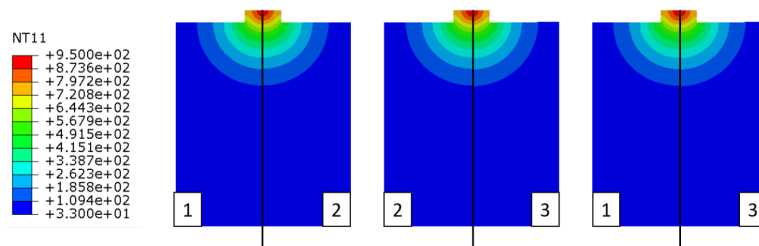
As seen in Figure 6, the mesh density influences the welding pool geometry and size. For the coarse mesh (1), the front of the pool is slightly wider with respect to results from other mesh densities: 0.26 mm

for 1–2 and 0.21 mm for 1–3 combinations. For the 2–3 combination, the fine mesh (3) is wider by approx. 0.1 mm. However, for the different mesh densities, the temperature distribution and weld pool shape seem to be different. Only for the 2–3 combination are the differences imperceptible. The mesh sensitivity was also evaluated for the substrate material, assuming the fine mesh for the sample. The finite element mesh setups, in this case, are collected in Table 3 and results in Figure 7.


**Fig. 6.** Temperature distributions in the AM samples for various combinations of mesh densities: coarse mesh – 1 ; medium mesh – 2; fine mesh – 3; a) top view; b) front view

**Table 3.** Parameters for simulations with the different bottom part element sizes

	Coarse mesh [mm] – 1	Medium mesh [mm] – 2	Fine mesh [mm] – 3
Sample	0.1025	0.1025	0.1025
Base	0.3	0.25	0.2


**Fig. 7.** Temperature distributions in the AM samples for various combinations of mesh densities in the base material: coarse mesh – 1; medium mesh – 2; fine mesh – 3; mesh for the printed part is fine

As presented, the temperature distribution profiles do not reveal visible differences. Therefore, a coarse mesh can be used for the substrate material, which will positively affect the computational time.

The final mesh (Fig. 8) consists of 857,088 and 386,400 finite elements for the sample and the base material, respectively.

The temperature field evolution during subsequent AM stages calculated with the developed FE model is presented in Figure 9. The comparison of the calculated and measured temperature profiles is summarized in Figure 10.

As presented, the predicted temperature profiles do not correspond well with the measurements. There-

fore, the theoretically calculated Goldak model parameters have to be fine-tuned with respect to the measurements from all the thermocouples.

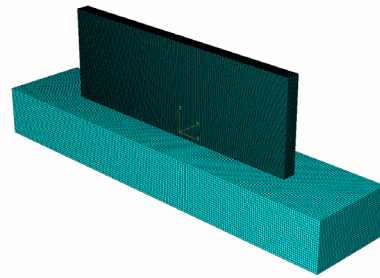


**Fig. 8.** 3D model and finite element mesh used for the numerical simulation of the AM process

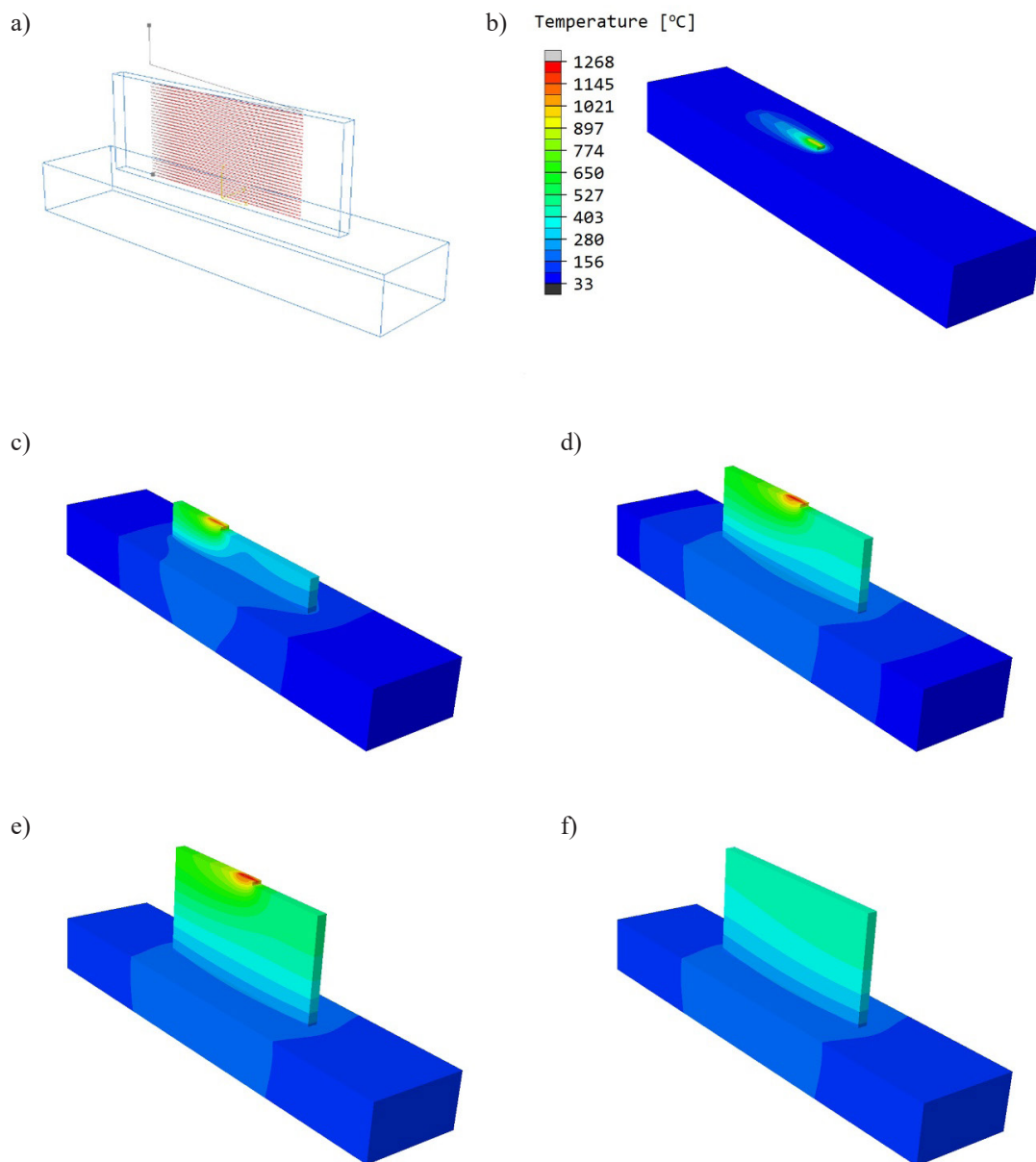


**Fig. 9.** Illustration of laser path (a) and temperature field evolution during subsequent AM stages calculated with the developed FE model in first layer (b), 11<sup>th</sup> layer (c), 22<sup>nd</sup> layer (d), 32<sup>nd</sup> layer (e), and final sample after printing (f)

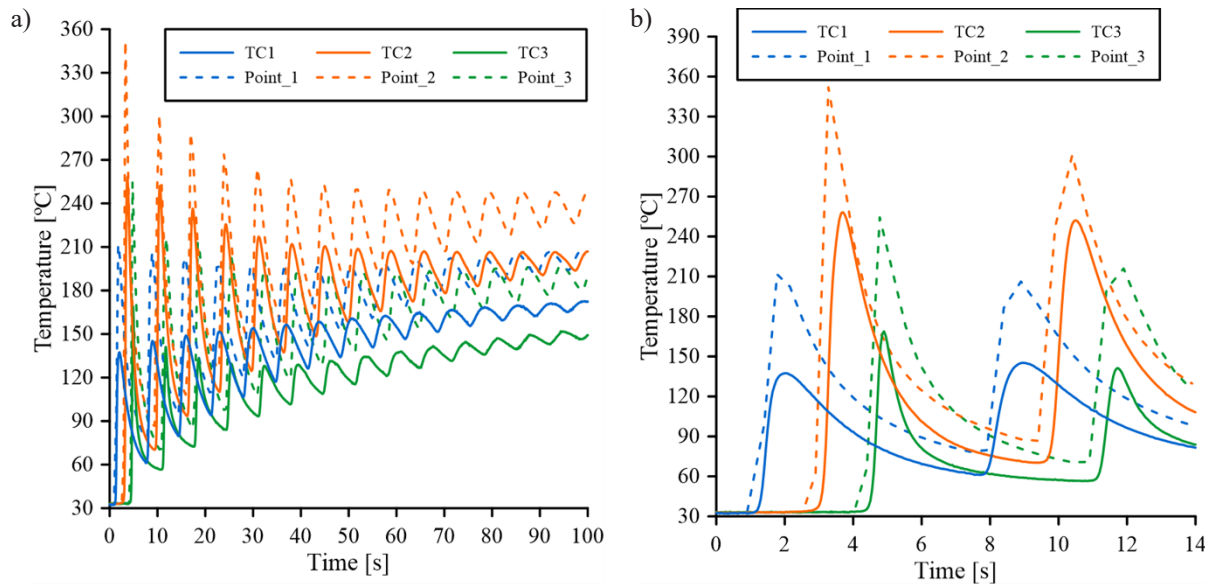


**Fig. 10.** The comparison of the calculated and measured temperature profiles during subsequent AM stages: a) 32 layers deposited; b) the first 2 layers deposited

#### 4. Fine-tuning of the Goldak model parameters

The influence of laser parameters on the shape of the welding pool and temperature profiles was investigated numerically and compared with the measurements in the point located approx. 1 mm from the top surface. Investigated simulation case studies are summarized in Table 4, while examples of obtained results are gathered in Figure 11.

**Table 4.** Modifications in values of the heat source parameters

	$a$ [mm]	$b$ [mm]	$c_f$ [mm]	$c_r$ [mm]
Initial setup				
	0.3	0.25	0.3	0.3
Investigated setups				
1	<b>0.15</b>	0.25	0.3	0.3
2	<b>0.45</b>	0.25	0.3	0.3
3	0.3	<b>0.1</b>	0.3	0.3
4	0.3	<b>0.4</b>	0.3	0.3
5	0.3	0.25	<b>0.15</b>	0.3
6	0.3	0.25	<b>0.45</b>	0.3
7	0.3	0.25	0.3	<b>0.15</b>
8	0.3	0.25	0.3	<b>0.45</b>

Results in Figure 11 show the influence of Goldak model parameters on temperature profiles at the examined points. As presented, parameters  $a$  and  $b$  have a small influence on the temperatures profiles. The only thing worth noting is that parameter  $a$  is responsible for

the depth and parameter  $b$  for the width of the bead. These two parameters are too small (0.15–0.45) to change largely the temperature 1 mm from the top surface. The maximal difference is in the 9.4 s of the simulation and is 0.1°C and 0.4°C for the parameter  $a$  and  $b$ , respectively. The front of the ellipsoid –  $c_f$  describes which element can be activated from the centre of the welding pool, and the  $c_r$  describes the length of the back part of the ellipsoid. Differences for parameters:  $c_f$  and  $c_r$  occur in the first temperature peak in the 3.275 s of the simulation. Smaller values for  $c_f$ , the same as larger values for  $c_r$ , give higher temperatures. For the first parameter, this may be due to a different element activation. Too early activated elements are taking part in heat transfer where heat is transported earlier to the surrounding air, where too late activated elements are not heated that well. Elements at the back of the ellipsoid are heated in a shorter or longer time, depending on the value for the  $c_r$  parameter.

During the further analysis of the results, a number of details were noticed. In the first simulation (Fig. 10), measured points for each layer were overheated. For Point 1 (left), the temperature started to rise from its minimum to 206°C, when in laboratory results, it is 136°C. Moreover, the minimal temperature after peak for Point 1 in the first layer was 78,5°C and 61°C in Abaqus and laboratory tests, respectively. This indicates that the wrong values of absorption coefficient and convective heat transfer coefficient were assumed. Thus, in the next step of the research, these material properties values and their impact on the temperature gradients were investigated.

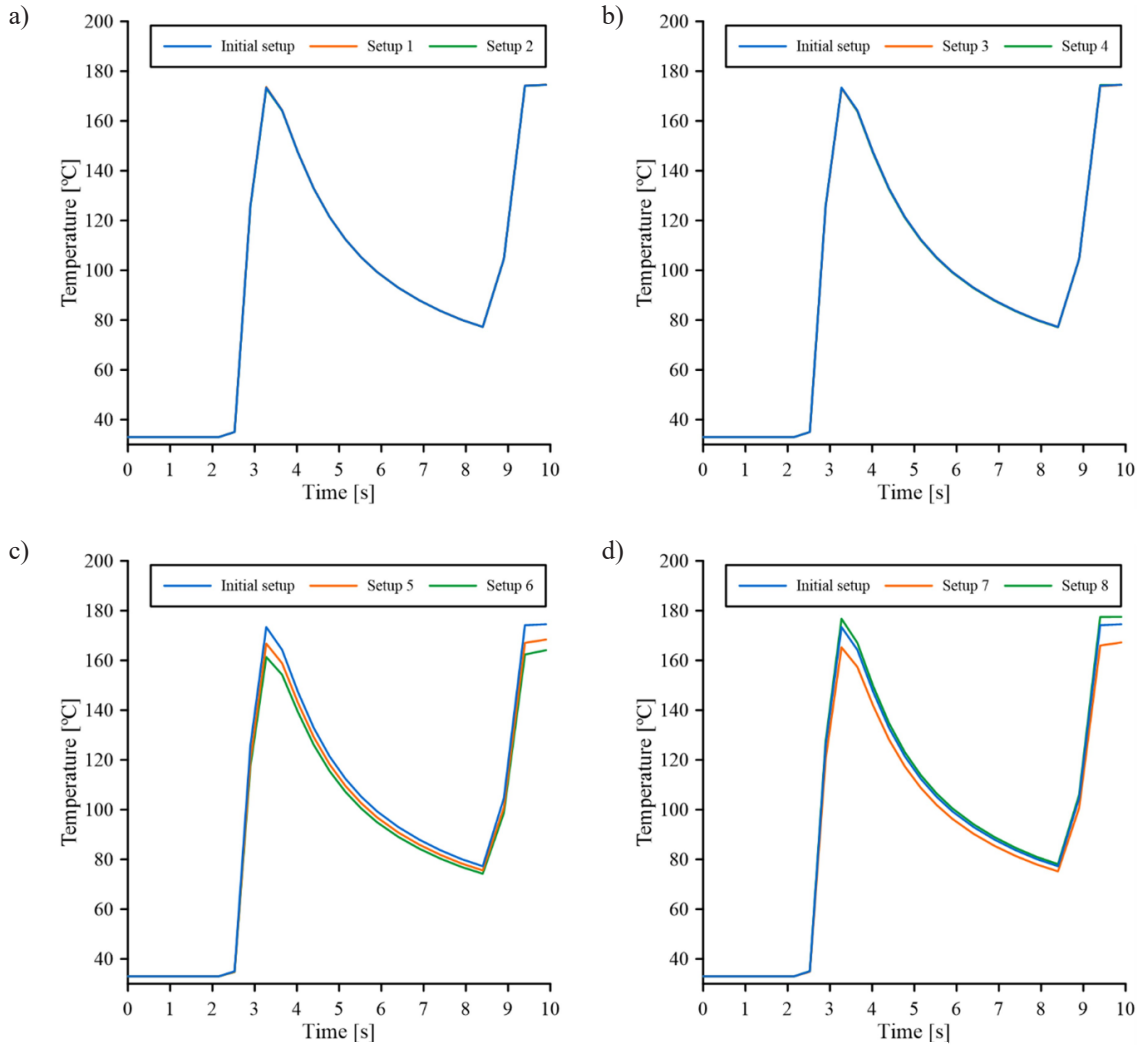


Fig. 11. Temperature profile changes measured in point (0; 0; -1) for 1–2 (a) , 3–4 (b), 5–6 (c), and 7–8 (d) case studies

The laser absorption coefficient is an important parameter in AM modelling. Due to the material of the powder and type of the absorption parameter (e.g., substrate, flat surface, spheres, and substrate), its values may vary even from 0.01 to 1 (Chen et al., 2007). In the current work, Inconel 718 was used. In this case, the wide spread in absorption coefficient value is observed in the literature (Boley et al., 2015). In Figure 12, temperature gradient dependence was presented for simulations with absorption coefficient  $\beta$  values equal to: 0.01, 0.15, and 0.36.

Similar to the absorption coefficient, a significant influence on the temperature evolution in the additive manufacturing parts has a convective heat transfer coefficient  $\alpha$  (Hochmann & Salehinia, 2018). Its value may vary depending on the process, examined location in the part, used gas, etc. (Foteinopoulos et al., 2018; Wang & Felicelli, 2006). Therefore, again three different values (0.01 mW/(mm<sup>2</sup>·K), 0.025 mW/(mm<sup>2</sup>·K) and 0.25 mW/(mm<sup>2</sup>·K)) were investigated as presented in Figure 13.

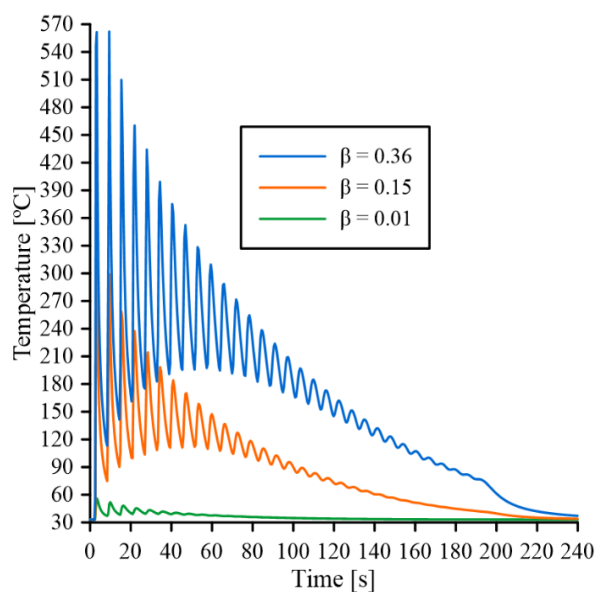
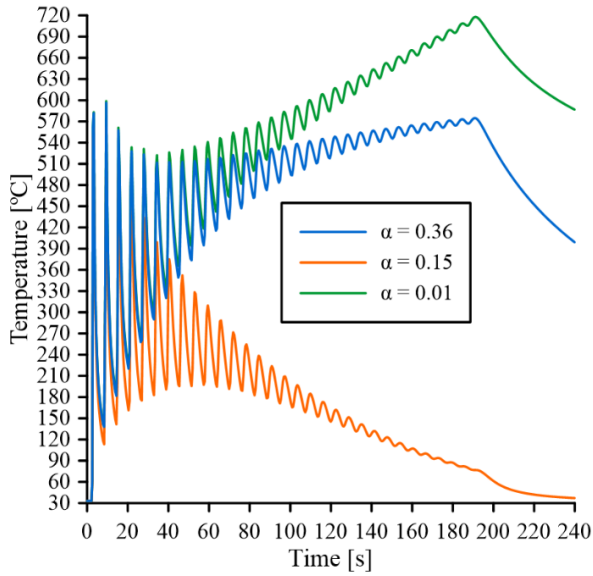


Fig. 12. Comparison of thermal cycle profiles for three absorption coefficient values



**Fig. 13.** Comparison of thermal cycle profiles for three convective heat transfer coefficients

As presented, identification of the appropriate value of the two mentioned coefficients is of importance. An inverse analysis based on the goal function related to the thermal cycle profiles was used during the identification procedure. After a series of numerical simulations, coefficients for the thermal model were established: absorption coefficient  $a = 0.11 \text{ mW}/(\text{mm}^2 \cdot \text{K})$  and convective heat transfer coefficient  $\alpha = 0.025 \text{ mW}/(\text{mm}^2 \cdot \text{K})$ . The best-identified solution during the inverse analysis is presented in Figure 14.

As presented, the thermal cycles are well mapped; only minor discrepancies are visible in Figure 14. These discrepancies are attributed to the simplifications introduced into the simulation. During this type of research, the sprayed powder is described as elements in the FE mesh, not as the small moving particles. The mesh size has a more negligible influence on the results, but if it is too coarse, the results can be disturbed due to overly early activation of FE elements. The thermocouple tip has a certain diameter that is also different from the element size in the FE mesh. Additionally, in the case of thermocouple measurements, there may be disturbances in the registration of thermal cycles. Nevertheless, in the practical application of the model, these simplifications do not strongly affect the quality of the prediction. The final identified FE model parameters for the AM process of Inconel 718 are summarized in Table 5.

**Table 5.** Identified FE model parameters for the AM process of Inconel 718

Laser parameters	$a$ [mm]	0.3
	$b$ [mm]	0.25
	$c_r$ [mm]	0.3
	$c_f$ [mm]	0.3
	$f_f$	1.0
	$f_r$	1.0
Thermal model parameters	$\beta$	0.11
	$\alpha$ [mW/(mm <sup>2</sup> ·K)]	0.025

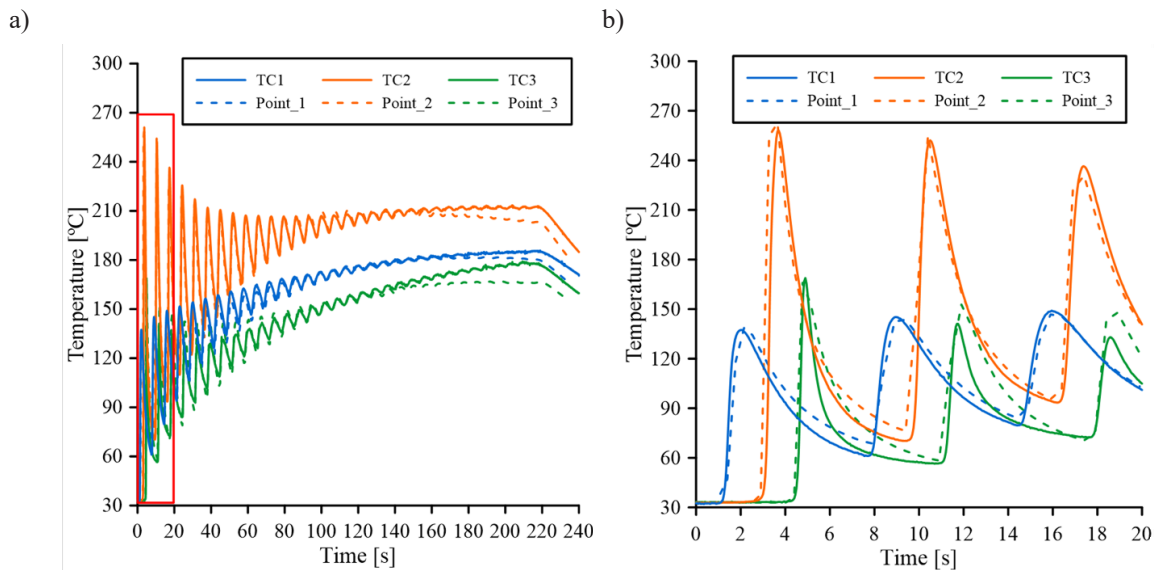


**Fig. 14.** Comparison of recorded and calculated thermal cycle profiles for LENS process: TC<sub>x</sub> – cycles recorded using thermocouples; Point<sub>x</sub> – cycles obtained from simulations using Abaqus; a) 32 layers deposited; b) the first 3 layers deposited

## 5. Conclusions

The main goal of this work was to identify the material and process parameters for the numerical simulation of the additive manufacturing process of Inconel 718. In the first step, a numerical finite element model replicating the LENS process setup was developed. The limitations of the theoretical approach to the calibration of the heat source model parameters were identified after the initial validation of model predictions with the experimental measurements. The sensitivity analysis study revalued the parameters that strongly influence the quality of FE model predictions. Some limitations of the experimental measurements of the

temperature profiles were also discussed. Finally, the inverse analysis technique provided a reliable set of process and material model coefficients that correctly replicate the character of the LENS process. Therefore, the identified set of parameters can be used for further numerical simulations with the mentioned laboratory stand.

## Acknowledgement

The work was realized as a part of fundamental research financed by the Ministry of Science and Higher Education, grant no. 16.16.110.663.

## References

- Bajaj, P., Hariharan, A., Kini, A., Kürnsteiner, P., Raabe, D., & Jäggle, E.A. (2020). Steels in additive manufacturing: A review of their microstructure and properties. *Materials Science and Engineering A*, 772, 138633. <https://doi.org/10.1016/j.msea.2019.138633>.
- Bergman, T., Lavine, A., Incropera, F., & DeWitt, D. (2011). *Introduction to Heat Transfer* (6 ed.). John Wiley & Sons.
- Bhandari, S., & Lopez-Anido, R.A. (2020). Discrete-event simulation thermal model for extrusion-based additive manufacturing of PLA and ABS. *Materials*, 13(21), 4985. <https://doi.org/10.3390/ma13214985>.
- Boley, C.D., Khairallah, S.A., & Rubenchik, A.M. (2015). Calculation of laser absorption by metal powders in additive manufacturing. *Applied Optics*, 54(9), 2477–2482. <https://doi.org/10.1364/AO.54.002477>.
- Brennan, M., Keist, J., & Palmer, T. (2020). Defects in Metal Additive Manufacturing Processes. In *Additive Manufacturing Processes* (vol. 24, pp. 277–286). ASM International. <https://doi.org/10.31399/asm.hb.v24.a0006557>.
- Calandri, M., Yin, S., Aldwell, B., Calignano, F., Lupoi, R., & Ugués, D. (2019). Texture and Microstructural Features at Different Length Scales in Inconel 718 Produced by Selective Laser Melting. *Materials*, 12(8), 1293. <https://doi.org/10.3390/ma12081293>.
- Chen, W.-L., Yang, Y.-C., & Lee, H.-L. (2007). Estimating the absorptivity in laser processing by inverse methodology. *Applied Mathematics and Computation*, 190(1), 712–721. <https://doi.org/10.1016/j.amc.2007.01.077>.
- Chiumenti, M., Cervera, M., Salmi, A., Agelet de Saracibar, C., Dialami, N., & Matsui, K. (2010). Finite element modeling of multi-pass welding and shaped metal deposition processes. *Computer Methods in Applied Mechanics and Engineering*, 199(37–40), 2343–2359. <https://doi.org/10.1016/J.CMA.2010.02.018>.
- Chua, B.L., Lee, H.J., Ahn, D.-G., & Wang, Y. (2019). A study on activation algorithm of finite elements for three-dimensional transient heat transfer analysis of directed energy deposition process. *International Journal of Precision Engineering and Manufacturing*, 20, 863–869. <https://doi.org/10.1007/s12541-019-00118-9>.
- Deng, D., Liang, W., & Murakawa, H. (2007). Determination of welding deformation in fillet-welded joint by means. *Journal of Materials Processing Technology*, 183(2–3), 219–225. <https://doi.org/10.1016/j.jmatprotec.2006.10.013>.
- Foteinopoulos, P., Papacharalampopoulos, A., & Stavropoulos, P. (2018). On thermal modeling of Additive Manufacturing processes. *CIRP Journal of Manufacturing Science and Technology*, 20, 66–83. <https://doi.org/10.1016/j.cirpj.2017.09.007>.
- Fu, G., Gu, J., Lourenco, M.I., Duan, M., & Estefen, S.F. (2015). Parameter determination of double-ellipsoidal heat source model and its application in the multi-pass welding process. *Ships and Offshore Structures*, 10(2), 204–217. <https://doi.org/10.1080/17445302.2014.937059>.
- Goldak, J., Chakravarti, A., & Bibby, M. (1984). A new finite element model for welding heat sources. *Metallurgical Transactions B*, 15, 299–305. <https://doi.org/10.1007/BF02667333>.
- Hochmann, E.A., & Salehinia, I. (2018). How convection on the substrate affects the thermal history of the build in direct laser deposition – finite element analysis. *The International Journal of Advanced Manufacturing Technology*, 96, 3471–3480. <https://doi.org/10.1007/s00170-018-1696-4>.
- Izadi, M., Farzaneh, A., Mohammed, M., Gibson, I., & Rolfe, B. (2020). A review of laser engineered net shaping (LENS) build and process parameters of metallic parts. *Rapid Prototyping Journal*, 26(6), 1059–1078. <https://doi.org/10.1108/RPJ-04-2018-0088>.
- Jiménez, M., Romero, L., Domínguez, I.A., Espinosa, M.D., & Domínguez, M. (2019). Additive manufacturing technologies: An overview about 3D printing methods and future prospects. *Complexity*, special iss. vol. 2019, <https://doi.org/10.1155/2019/9656938>.
- Kik, T. (2020). Computational techniques in numerical simulations of arc and laser welding processes. *Materials*, 13(3), 608. <https://doi.org/10.3390/ma13030608>.

- Kodama, H. (1981). Automatic method for fabricating a three-dimensional plastic model with photo-hardening polymer. *Review of Scientific Instruments*, 52(11), 1770. <https://doi.org/10.1063/1.1136492>.
- Malmelöv, A. (2016). *Modeling of additive manufacturing with reduced computational effort* [master's thesis]. Luleå University of Technology.
- Pereira, J.C., Aranzabe, J., Taboada, M.C., Ruiz, N., & Rodriguez, P.P. (2021). Analysis of microstructure and mechanical properties in as-built/as-cast and heat-treated conditions for IN718 alloy obtained by selective laser melting and investment casting processes. *Crystals*, 11, 1196. <https://doi.org/10.3390/cryst11101196>.
- Petrovic, V., Gonzalez, J.V.H., Ferrando, O.J., Gordillo, J.D., Puchades, J.R.B., & Grinan, L.P. (2011). Additive layered manufacturing: Sectors of industrial application shown through case studies. *International Journal of Production Research*, 49(4), 1061–1079. <https://doi.org/10.1080/00207540903479786>.
- Stender, M.E., Beghini, L.L., Sugar, J.D., Veilleux, M.G., Subia, S.R., Smith, T.R., San Marchi, Ch.W., Brown, A.A., Dagle, D.J. (2018). A thermal-mechanical finite element workflow for directed energy deposition additive manufacturing process modeling. *Additive Manufacturing*, 21, 556–566. <https://doi.org/10.1016/j.addma.2018.04.012>.
- Wang, L., & Felicelli, S. (2006). Study of heat transfer mechanisms during the LENS™ process. *AMPT. Advances in Materials and Processing Technologies. July 30 – August 3, Las Vegas Nevada*. <https://citeseerx.ist.psu.edu/viewdoc/download?doi=10.1.1.522.6208&rep=rep1&type=pdf>.
- Wohlers, T.T., Campbell I., Diegel O., Huff R., & Kowen, J. (2020). *3D Printing and Additive Manufacturing Global State of the Industry*. Wohlers Associates.
- Ye, R., Smugeresky, J.E., Zheng, B., Zhou, Y., & Lavernia, E.J. (2006). Numerical modeling of the thermal behavior during the LENS process. *Materials Science and Engineering A*, 428(1–2), 47–53. <https://doi.org/10.1016/j.msea.2006.04.079>.

